Science and Technology of Advanced Materials

ISSN: 1468-6996 (Print) 1878-5514 (Online) Journal homepage: www.tandfonline.com/journals/tsta20

High thermoelectric performance of p-type $Fe_2V_{0.8}Mn_{0.2}Al$ Heusler alloy thin films grown on insulating oxide substrates

Rajveer Jha, Naohito Tsujii, Alexander Riss, Michael Parzer, Ernst Bauer, Takahiro Baba & Takao Mori

To cite this article: Rajveer Jha, Naohito Tsujii, Alexander Riss, Michael Parzer, Ernst Bauer, Takahiro Baba & Takao Mori (2025) High thermoelectric performance of p-type $Fe_2V_{0.8}Mn_{0.2}Al$ Heusler alloy thin films grown on insulating oxide substrates, Science and Technology of Advanced Materials, 26:1, 2512705, DOI: 10.1080/14686996.2025.2512705

To link to this article: https://doi.org/10.1080/14686996.2025.2512705

SCIENCE AND TECHNOLOGY OF ADVANCED MATERIALS
2025, VOL. 26, NO. 1, 2512705
https://doi.org/10.1080/14686996.2025.2512705

Taylor & Francis
Taylor & Francis Group

FOCUS ISSUE ARTICLE

OPEN ACCESS Check for updates

High thermoelectric performance of p-type $Fe_2V_{0.8}Mn_{0.2}Al$ Heusler alloy thin films grown on insulating oxide substrates

Rajveer Jha[a], Naohito Tsujii[a], Alexander Riss[b], Michael Parzer[b], Ernst Bauer[b], Takahiro Baba[a,c] and Takao Mori[a,c]

[a]Research Center for Materials Nanoarchitectonics (MANA), National Institute for Materials Science (NIMS), Tsukuba, Japan;
[b]Institute of Solid State Physics, Technische Universität Wien, Vienna, Austria;
[c]Graduate School of Pure and Applied Sciences, University of Tsukuba, Tsukuba, Japan

ABSTRACT

High-performance thermoelectric (TE) materials near room temperature are crucial for cooling and energy harvesting applications. This study reports the outstanding thermoelectric performance of *p*-type Mn-doped Fe_2VAl Heusler alloy thin films, specifically $Fe_2V_{0.8}Mn_{0.2}Al$, prepared using magnetron sputtering. These films were deposited on insulating oxide substrates to eliminate any spurious contributions from the substrate. Large *p*-type Seebeck coefficients (S) have been observed for all films, revealing a maximum power factor of 4.26 $mWK^{-2}m^{-1}$ at 300 K. This study revealed thickness-dependent thermoelectric properties, with the highest power factor achieved in the 500 nm film. Films with d = 300 nm and 500 nm exhibit weak ferromagnetism. Hall resistivity measurements evidence an anomalous Hall effect (AHE) for the 300 nm and 500 nm samples. The AHE is strongest for the 500 nm film, consistent with a magnetic enhancement of the Seebeck coefficient and power factor. Additionally, we synthesized Al-rich p-type $Fe_2V_{0.9}Mn_{0.1}Al_{1.5}$ thin films at room temperature, 200°C, 400°C, and 600°C. The film deposited at 600°C exhibits an exceptional figure of merit ZT_{appr} ~0.8 and a power factor of 6.7 $mW{\cdot}K^{-2}{\cdot}m^{-1}$ at room temperature, which are respectively, 4 times and 1.5 times larger than the best values ever reported for any bulk or thin film *p*-type Fe_2VAl-based material.

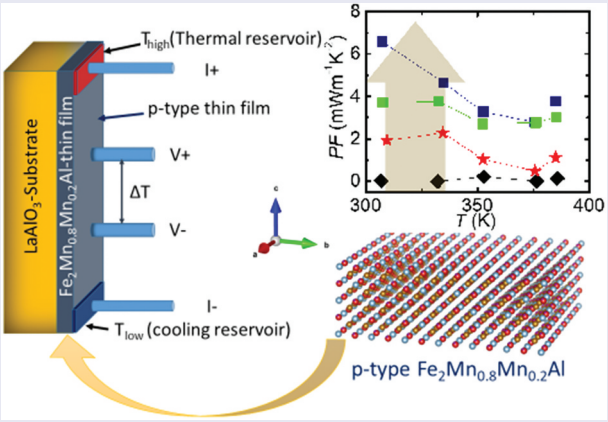

Thin films of p-type Mn-doped Fe_2VAl Heusler alloy achieving highest power factor of any materials *p*-type thin film.

IMPACT STATEMENT

The performance of p-type Fe2VAL has traditionally lagged far behind the n-type. In this work, exceptionally high thermoelectric performance in p-type Mn-doped Fe2VAl Heusler alloy thin films were achieved.

ARTICLE HISTORY
Received 10 March 2025
Accepted 23 May 2025
Revised 21 May 2025

KEYWORDS
Thin films; heusler alloys; electrical resistivity; Seebeck coefficient; thermal conductivity; *ZT*

Introduction

Thermoelectric (TE) materials offer a promising solution for generating eco-friendly electricity, addressing current energy challenges. A thermoelectric generator can convert waste heat into electricity [1,2]. Especially for smaller heat sources, low-power applications in the Internet of Things (IoT) are anticipated [3]. Therefore, enhancing the conversion efficiency of thermoelectric

CONTACT Naohito Tsujii TSUJII.Naohito@nims.go.jp; Takao Mori MORI.Takao@nims.go.jp Research Center for Materials Nanoarchitectonics (MANA), National Institute for Materials Science (NIMS), Namiki 1-1, Tsukuba 305-0044, Japan
Supplemental data for this article can be accessed online at https://doi.org/10.1080/14686996.2025.2512705

materials is a critical objective [4,5]. The efficiency of thermoelectric materials is characterized by the dimensionless figure of merit ($ZT = S^2/\rho\kappa \cdot T$), where S is the Seebeck coefficient, ρ is the electrical resistivity, κ ($\kappa_e + \kappa_{ph}$) is the total thermal conductivity, and T is the temperature. Traditional TE materials like Bi_2Te_3, SiGe, and PbTe have consistently attracted attention for their high thermoelectric performance and have been successfully used in various applications, like geothermal energy harvesting, stove fans in radioisotope thermoelectric generators for deep space probes [5–7].

In recent years, the demand for new high-performance TE materials, such as Mg_3Sb_2, has spurred numerous studies, resulting in continually improved zT values through various strategies [8,9]. Several methods, including doping, atomic-scale alloying, nano- and mesoscale structuring, matrix or inclusion band alignment, and intra-matrix electronic structure engineering, have been proposed to enhance the parameters ρ, κ, and S [4,8–12]. However, other important parameters like the chemical and physical stability of TE materials have often been neglected. Here, intermetallic half- and full-Heusler materials pose a promising alternative as they exhibit good stability and reasonably cheap constituent elements combined with good TE performance. For TE applications close to room temperature, especially full-Heusler materials, have shown great potential. Thin film deposition of TE materials constitutes a favorable technique to further increase ZT and enable microscale applications. Recently, B. Hinterleitner et al. reported a large Seebeck coefficient and a significant power factor in Heusler alloy thin films [13]. Thin films of n-type $Fe_2V_{0.8}W_{0.2}Al$ deposited on Si substrates exhibited high power factors, exceeding 45 $mW{\cdot}m^{-1}{\cdot}K^{-2}$, and a ZT around 5, which represents excellent thermoelectric performance for future applications [13]. In contrast, W-doped $Fe_2V_{0.8}W_{0.2}Al$ bulk polycrystalline samples have a power factor of around 5 $mW{\cdot}m^{-1}{\cdot}K^{-2}$ [14]. Hence, the film's power factor is several times larger than that of the bulk sample, indicating a significant potential for improving the performance of TE materials. p-type full-Heusler thin films with similar TE properties, however, are still lacking. Hence, this report focuses on the deposition of p-type Fe_2VAl-based thin films on insulating $LaAlO_3$ substrates.

In its bulk form, ternary Fe_2VAl has garnered significant attention for thermoelectric power generation near room temperature [15]. Fe_2VAl is characterized as having a low carrier density, nonmagnetic, and compensated semimetal – key properties which make it promising for thermoelectric application [16–19]. Theoretical calculations consistently report on a deep pseudogap at the Fermi level of Fe_2VAl [20–23]. This deep pseudogap has been confirmed through nuclear magnetic resonance studies, optical conductivity, and photoemission spectroscopy measurements [24–26]. Nevertheless, recent studies suggest that an indirect narrow-band-gap semiconductor is a more accurate description of the Fe_2VAl system [27,28]. Regardless of this debate, the semimetallic (small-bandgap) electronic structure provides two types of carriers, i.e. electrons and holes, resulting in a compensated and relatively small Seebeck coefficient in undoped Fe_2VAl [6]. Hence, intentional doping in the Fe_2VAl system is essential to obtain optimized n-type or p-type systems with excellent thermoelectric properties [17–19,29–35].

Additionally, leveraging magnetism to enhance the Seebeck coefficient is increasingly recognized as a promising strategy, as evidenced by recent efforts involving magnon drag, paramagnon drag, spin fluctuations, and spin entropy [36–43]. Magnetic interactions for thermoelectric power generation, such as the spin Seebeck effect, anomalous Nernst effect, and magnon-drag thermopower, are also receiving significant attention [44–49]. It is well known that magnon- or spin-related effects are characterized by thermally non-equilibrium spin currents, mainly due to spatially localized electrons and are effective only in the magnetically ordered state. However, magnon drag theory can help explain spin fluctuation enhancements in itinerant electron systems, which are effective even in the paramagnetic state. While stoichiometric Fe_2VAl is non-magnetic due to its compensated, semimetallic ground state, slight variations of its composition facilitate various magnetic defects, interacting with conduction electrons and eventually leading to a half-metallic, magnetic ground state for larger substitutions, when deviating from a valence electron count VEC = 6 per atom.

To exploit these magnetic interactions and optimize the TE performance of Fe_2VAl, in the present study, we have synthesized Mn-doped $Fe_2V_{0.9}Mn_{0.2}Al$ and $Fe_2V_{0.9}Mn_{0.1}Al_{1.5}$ thin films. For p-type $Fe_2V_{0.8}Mn_{0.2}Al$ films we find good thermoelectric properties, a high-power factor, PF ~4.26 $mWm^{-1}K^{-2}$, with high Seebeck coefficient, low electrical resistivity, and relatively low thermal conductivity, culminating to $ZT_{appr} = 0.4$ at RT, which we trace back to an enhancement via spin fluctuations, supported by additional magnetic and Hall effect measurements. In addition, even larger power factors of up to 6.5 mWm^{-1} K^{-2} are derived for off-stoichiometric $Fe_2V_{0.9}Mn_{0.1}Al_{1.5}$ films and explored with respect to their deposition temperatures (20°C, 200°C, 400°C, and 600°C). The thermoelectric figure-of-merit of the film deposited at 600°C attains record-high values of $ZT_{appr} = 0.8$ close to room temperature, marking one of the highest ZT of any p-type thin film thermoelectric material at these temperatures.

Experimental methods

Appropriate amounts of Fe (99.98%), V (99.9%), Mn (99.99%), and Al (99.999%) were weighed in and melted in an arc furnace under an argon atmosphere, according to the nominal compositions $Fe_2V_{0.8}Mn_{0.2}Al$ and $Fe_2V_{0.9}Mn_{0.1}Al_{1.5}$. The melted ingots were quenched in a water-cooled copper crucible and re-melted at least four times to ensure homogeneity. The ingots were then loaded one by one into a tungsten carbide jar in the glovebox and milled to a fine powder using planetary ball milling at a speed of 350 rpm for 4 hours. These fine powders were consolidated by spark plasma sintering (SPS, SPS-1080 System, SPS SYNTEX INC, USA) under a pressure of 60 MPa at 1273 K for 10 minutes in a dynamic vacuum. The diameter of the graphite die used for fabricating the sputtering target was 2 inches.

Thin films with a nominal composition of $Fe_2V_{0.8}Mn_{0.2}Al$ were grown at a substrate temperature of 873 K using the radio frequency magnetron sputtering technique in a commercially designed apparatus purchased from Giko Inc (Japan). Single-side polished fused $LaAlO_3$ (10 mm × 10 mm × 1 mm) served as substrates. The background pressure in the deposition chamber and the working pressure of argon gas were set to less than 4.0×10^{-5} Pa and 0.04 Pa, respectively. The thin film samples were deposited under 50 W RF power for about 60 minutes to achieve a film thickness of approximately 500 nm. After deposition, the films were annealed at 873 K for 24 hours. For the deposition technique magnetron sputtering, the deposition power, substrate temperature, working pressure, and Ar flow rate were selected based on prior optimization studies and preliminary experiments to achieve dense, uniform films with controlled stoichiometry. Specifically, the sputtering power was chosen to balance deposition rate with minimal target damage, while the substrate temperature was set to promote atom mobility without inducing unwanted crystallization during deposition. The working pressure affects the mean free path of sputtered atoms, which influences film morphology; hence, a moderate pressure was used to ensure good film density. Regarding annealing treatment, the temperature and duration were optimized to promote phase formation and crystallinity without inducing film delamination or excessive grain growth.Powder X-ray diffraction was performed to determine the crystal structure using a RINT TTR-3 diffractometer (Rigaku Co., Akishima, Tokyo, Japan) with Cu-Kα radiation. Bar-shaped samples were used to measure the Seebeck coefficient and electrical resistivity. These measurements were done using a four-probe method with a commercial system (ZEM3, Advance Riko Inc., Japan). The thermal conductivity (κ) was calculated using $\kappa = \alpha \cdot c_p \cdot \rho$, where α is the thermal diffusivity, c_p is the specific heat capacity, and ρ is the density. The thermal diffusivity coefficient (α) and the heat capacity (c_p) of the bulk material were simultaneously measured for the disk sample using a xenon flash system (Netzsch LFA 467, Germany) with a pyro Ceram disk as a reference sample. The thermal diffusivity of thin films with a thickness of around 500 nm was measured by applying the nanosecond time-domain technique using NanoTR (PicoTherm, NETZSCH, Japan) based on the rear heat-front detect configuration. Specific heat and sample density data of bulk $Fe_2V_{0.8}Mn_{0.2}Al$ were used as a first approximation for the thin-film values.

The microstructure and composition analyses were characterized using a field emission scanning electron microscope (FESEM, Hitachi S-4800, Japan) equipped with an energy dispersive spectrometer (EDS, Horiba EMAXEvolution X-Max, Japan) and transmission electron microscopy (TEM, JEOL Inc., USA). Magnetization measurements were performed employing a MPMS (magnetic property measurement system), a superconducting quantum interference device magnetometer from Quantum Design (USA). The Hall resistivity was measured using a Quantum Design (USA) PPMS (Physical Property Measurement System).

Structural analysis

In order to appropriately characterize the crystal structure, phase purity as well as the grain structure and morphology of Fe_2VAl-based full-Heusler alloys, X-ray diffraction (XRD) studies at room temperature, scanning electron microscopy (SEM) and electron backscattering diffraction (EBSD) techniques were employed.

1. Thickness dependent structural features of of $Fe_2V_{0.8}Mn_{0.2}Al$

Figure 1(a) show the XRD patterns obtained for $Fe_2V_{0.8}Mn_{0.2}Al$ thin films for various thicknesses. Films with thicknesses of $d = 200$ nm and 500 nm were found to crystallize in a highly symmetric cubic $L2_1$-structure (space group Fm-3 m). The respective XRD patterns were indexed accordingly, and the (111) and (200) peaks are clearly observed for these samples. This observation is a clear indicator for the presence of the classical full-Heusler structure. The high-intensity peaks observed for the 500 nm thin film suggest a high degree of crystallinity, indicating the structure to be fully ordered.

In contrast, the (111) peak is absent in the samples with thicknesses of 100 nm and 300 nm, which may be attributed to a strong texture effect. However, the possibility of a partially disordered structure in these films cannot be entirely ruled out. In addition, for

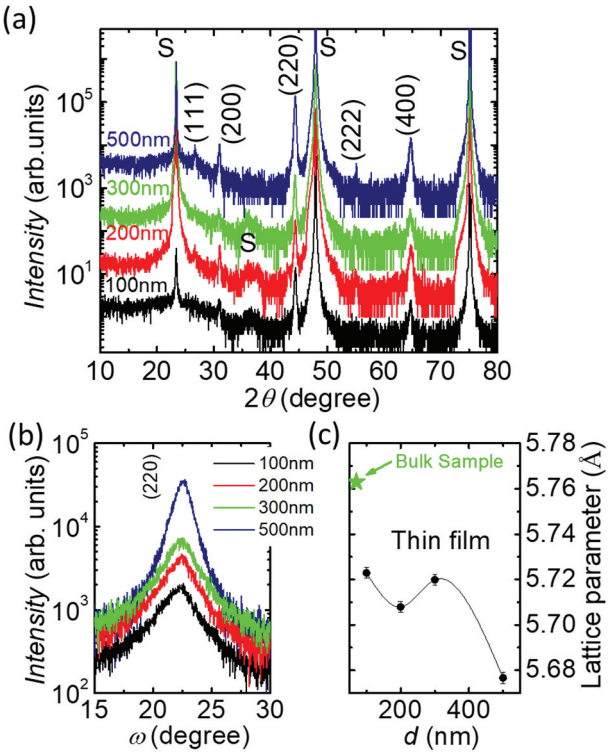

Figure 1. (a) X-ray diffraction pattern of $Fe_2V_{0.8}Mn_{0.2}Al$ thin films of thickness 100 nm, 200 nm, 300 nm, and 500 nm. Here, *S* is symbolized as $LaAlO_3$ substrate. (b) ω-scan XRD pattern. (c) Lattice parameters vs. thickness as obtained from the (220) peak.

Heusler compounds, the absence of the (111) peak is generally associated with antisite disorder, particularly involving Fe/Al or Fe/V atomic exchanges, which is typical for full-Heusler structures [50]. Antisite defects due to the interchange of Fe_V and Fe_{Al} have larger formation energies and thus, are less prominent [51].

Furthermore, an ω scan was performed for all films for the fixed peak position (220) see Figure 1(b). The peak intensity decreases with decreasing thickness of the samples. Also, ω scans were done for the (111) and (200) peaks (see Fig. S1). The intensity of the (111) and (200) peaks is largest for the 500 nm sample. The (111) peak is clearly seen for 200 nm, 300 nm, and 500 nm films. However, the (111) peak is missing for the 100 nm thin film; thus, the structure is likely of the CsCl type [52]. The lattice parameters obtained are displayed in Figure 1(c). The lattice parameter of the $Fe_2V_{0.8}Mn_{0.2}Al$ thin films of various thicknesses was calculated from the (220) peak using Bragg's law. It was found to be 5.676 ± 0.002 for the 500 nm thin film. The error bar was obtained from peak fitting uncertainty and propagated through the interplanar spacing formula. Obviously, the lattice parameters of the structurally ordered films, by trend, are lower than the ones of the disordered films. For comparison, the lattice parameter ($a = 5.764$ Å) of bulk $Fe_2V_{0.8}Mn_{0.2}Al$ is shown, too, being larger than that of all thin film samples. Overall, the lattice parameter is lowest for the 500 nm sample, which may reflect residual strain effects commonly associated with thin film growth on mismatched substrates such as $LaAlO_3$. Rather than assuming a specific epitaxial relationship, we attribute the observed deviation from the bulk lattice parameter to factors such as thermal stress arising from differences in thermal expansion coefficients between the film and substrate, intrinsic stress generated during the sputtering process, and potential compositional variations. These factors can alter the film's structural properties and may, in turn, influence its electronic or magnetic behavior.

Figure 2(a) shows a cross-sectional SEM image of the $Fe_2V_{0.8}Mn_{0.2}Al$ film, confirming the thickness to be around 500 nm. SEM and EDS measurements were performed to examine the morphology and composition of the grown thin films. Figure 2(b) presents the morphology of the 1 μm thin film, revealing a smooth surface. EDS data were collected from $d = 1$ μm film deposited on a Si substrate to avoid inaccurate evaluation, such as the inclusion of Al from $LaAlO_3$ substrates. The film was prepared under the same deposition conditions as all other films used for thermoelectric and structural properties analysis. The inset of Figure 2(b) reveals the EDS mapping image, indicating a uniform elemental distribution. The actual chemical composition, determined by EDS, is shown in Table 1, with the thin films being slightly V-deficient and Al-rich. Minor off-stoichiometry in the chemical composition of thin films suggests a preferential sputtering effect, which, however, can distinctly affect thermoelectric properties.

Figure 2(c,d) show high-magnification SEM images of the topography of the 300 nm and 500 nm films, respectively. The grain size of the 500 nm film is larger than that of the 300 nm film. Grains, in general, markedly affect the scattering of charge carriers and phonons. SEM images showing the topography of the 100 nm and 200 nm thin films are presented in supplementary information Fig. S2(a) and S2(b), respectively.

EBSD data are summarized in the supplementary information, Fig. S3, revealing distinct grain boundaries with excellent connectivity. EBSD confirms the larger grain size of the 500 nm sample, compared to the 300 nm film.

2. Structural features of substrate-temperature dependent $Fe_2V_{0.9}Mn_{0.1}Al_{1.5}$ films

Al-rich $Fe_2V_{0.9}Mn_{0.1}Al_{1.5}$ thin films with $d = 500$ nm were prepared, using different deposition temperatures, varying from room temperature (RT) to $T_{dep} = 600$°C. Figure 3 shows the respective XRD patterns for the films deposited at various temperatures. The peaks observed for RT and 200°C, at ~15° and ~38°, correspond to artifacts from the substrate. Films deposited at RT and 200°C exhibit the (220) peak; the (111) and

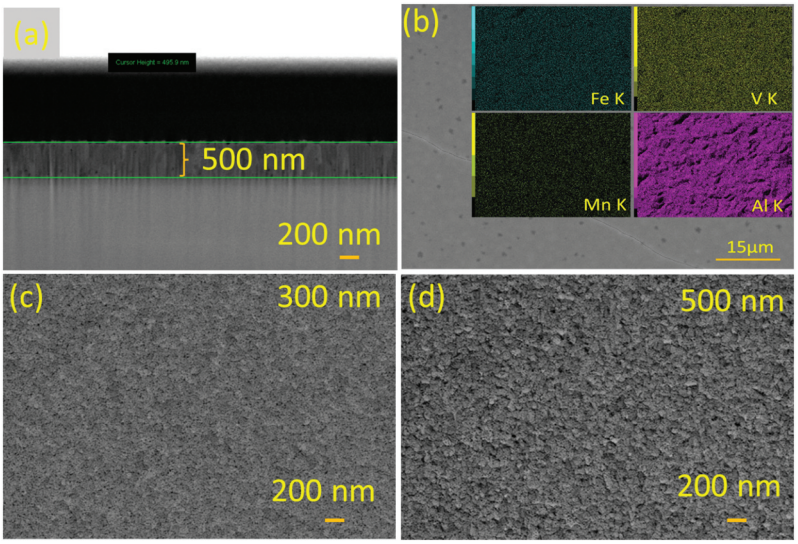

Figure 2. Microstructure characterization of $Fe_2V_{0.8}Mn_{0.2}Al$ thin films of 300 nm and 500 nm thickness; (a) cross-section SEM image; (b) SEM-EDS analysis of the selected area of $Fe_2V_{0.8}Mn_{0.2}Al$ thin films; (c,d) high magnification SEM images of thin films of 300 nm and 500 nm thickness.

Table 1. SEM+EDS elemental analysis for fabricated target and thin film, the selected area for composition analysis is about $50 \times 50\ \mu m^2$.

Sample	Fe	V	Mn	Al
Nominal composition	50	20	5	25
Target composition	49.9	19.8	5.1	25.2
Thin film composition	49.5	18.53	5.47	26.5

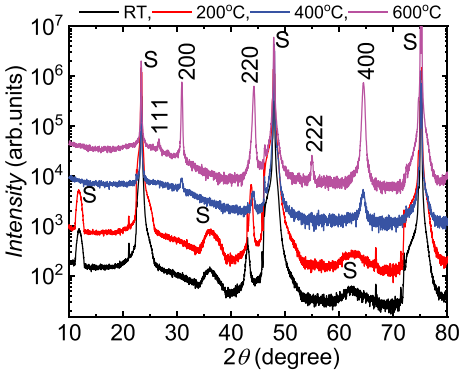

Figure 3. X-ray diffraction pattern of $Fe_2V_{0.9}Mn_{0.1}Al_{1.5}$ thin films deposited at different temperatures; RT, 200°C, 400°C, and 600°C, respectively. Here, RT and *S* are symbolized as room temperature and substrate, respectively.

(200) reflections, however, are missing entirely. As already mentioned in the previous section, this observation indicates a fully disordered crystalline unit cell, i.e. all atoms can occupy all atomic positions of the crystal structure. In this very extreme case, a W-type structure results, which might cause large resistivity values, because of a maximal degree of disorder. Oppositely, the film deposited at 400°C reveals the (200) peak, while the 600°C film, in addition, displays the (100) peak, too.

This observation indicates increased structural order with increasing substrate temperatures, resulting in the fully ordered classical full-Heusler structure for the 600°C sample. Figure 3 shows that the (200) peak is much higher in intensity than the (200) expected from the poly-crystalline Heusler phase. This suggests that the (200) planes are more dominant than theoretically expected, hinting towards preferred orientation of grains. The preferential orientation obtained here for $Fe_2V_{0.9}Mn_{0.1}Al_{1.5}$ is much more prominent than that of the $Fe_2V_{0.8}Mn_{0.2}Al$ films, as studied in the previous section. The unequal orientation of specific crystallographic planes can influence the carrier mobility along different directions and may modify the thermoelectric performance of thin films.

Thermoelectric properties

To assess the thermoelectric figure of merit, we have measured the temperature dependence of the Seebeck coefficient (S) and the electrical conductivity (σ) of all fabricated thin films in the temperature range 300–600 K. Since measuring the thermal conductivity of thin films is challenging due to substrate contributions, we measured the total thermal conductivity (κ) at room temperature and extrapolated the electronic part of κ (κ_e) to higher temperatures using $\sigma(T)$ and applying the Wiedemann-Franz law ($\kappa_e = L\sigma T$). The measurement techniques employed are described in the *Experimental methods* section above.

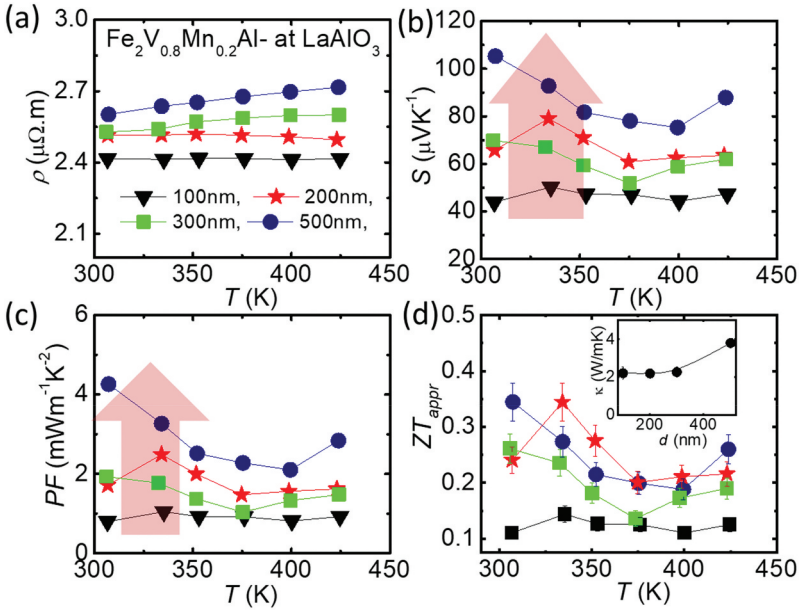

Figure 4. Electrical transport properties of $Fe_2V_{0.8}Mn_{0.2}Al$ thin films of thicknesses 100 nm, 200 nm, 300 nm, and 500 nm; (a) electrical resistivity ρ, (b) Seebeck coefficient S, (c) the power factor *PF*, and (d) the figure of merit ZT_{appr}.

1. Thermoelectric properties of $Fe_2V_{0.8}Mn_{0.2}Al$ films for varying film thicknesses

Figure 4(a-d) summarize the temperature-dependent thermoelectric properties of four $Fe_2V_{0.8}Mn_{0.2}Al$ films of different thicknesses. The electrical resistivity, $\rho(T)$, of the 100 nm and 200 nm films is nearly temperature-independent, whereas the 300 nm and 500 nm films exhibit weak temperature dependencies. Notably, the overall electrical resistivity of the films is lowered by a factor of 2 compared to $\rho(T)$ of the bulk $Fe_2V_{0.8}Mn_{0.2}Al$ [53].

The metallic-like electrical resistivity observed for the films is likely due to carrier doping caused by a slight off-stoichiometry owing to the sputtering process. Another factor influencing the electrical resistivity might be related to disorder, the grain size and the grain boundary formation in the $Fe_2V_{0.8}Mn_{0.2}Al$ films, as discussed in the *Structural analysis* section.

The Seebeck coefficient *S*(T) of the $Fe_2V_{0.8}Mn_{0.2}Al$ film with $d = 500$ nm exhibits large positive values, indicating that holes are the majority charge carriers. While the overall resistivity rises with the film thickness, the Seebeck coefficient is highest for those samples exhibiting a higher degree of $L2_1$ ordering in their XRD pattern. *S(T)* of the 500 nm and 200 nm films is larger than *S(T)* of the 300 nm and 100 nm samples. A possible explanation for these differences in *S*(*T*) are the different levels of ordering present in the films, leading to a variation of the effective electronic structure. At room temperature, the Seebeck coefficient of the 500 nm film reaches up to $S = 108$ μV/K, decreasing with increasing temperature, suggesting contributions of bipolar conduction at these temperatures.

The power factor, $PF = S^2/\rho$, defines the electronic part of the thermoelectric figure of merit, comprising the electrical resistivity and Seebeck coefficient. As shown in Figure 4(c), the power factor obtains values of up to $PF = 4.26$ $mWK^{-2}m^{-1}$ for the 500 nm film at $T = 300$ K, which is one of the highest values among *p*-type Heusler materials and the yet highest for *p*-type thin films. In comparison, a power factor of 2.8 $mWK^{-2}m^{-1}$ has been found at 325 K for the 200 nm thin film and about half of that for the 100 nm sample, due to the substantially lower Seebeck coefficients.

The thermal conductivity of the thin films in the cross-plane direction was measured, using the pico-second time-domain thermoreflectance (TD-TR) technique. For these measurements, the rear-heat front-detect (RF) configuration was employed [54]. The measured time-dependent thermoreflectance signals of the thin film samples (100 nm, 200 nm, 300 nm, and 500 nm) at room temperature are shown in Fig. S4. For the analysis, the mirror-image method is used [for details see supplementary information] [54]. The model was fitted to the thermoreflectance signals in order to estimate two key parameters: τ_f (the relaxation time of the thin film) and γ (a parameter related to the system's response). These parameters were determined by curve fitting, allowing the model to capture the dynamics of the thermal response of the film [55]. Because d_f (the film's thickness) was already known, the thermal diffusivity α_f of the thin film could be determined based on the fitted model. Using the thermal diffusivity and the known specific heat capacity c_{bulk} and density ρ_{bulk} of the material, the thermal conductivity κ was then calculated via the equation:

$$\kappa = \alpha_f c_{bulk} \rho_{fbulk}.$$

Where c_{bulk} and ρ_{bulk} are specific heat capacity and density of $Fe_2V_{0.8}Mn_{0.2}Al$ bulk material, respectively (c_{bulk} = 467[J/(kg·K)], ρ_{bulk} = 6590[kg/m^3]) [56]. From the time-dependent thermoreflectance signals and analysis, the obtained thermal conductivities for the films are 3.80 $Wm^{-1}K^{-1}$ for the 500 nm film, 2.26 $Wm^{-1}K^{-1}$ for the 300 nm film, 2.19 $Wm^{-1}K^{-1}$ for the 200 nm film, and 2.21 $Wm^{-1}K^{-1}$ for the 100 nm film, respectively. In this study, we have used bulk values for density and specific heat capacity as approximations in the calculation of the thermal conductivity and the derived thermoelectric figure of merit (ZT). This approach was adopted due to the lack of direct measurements for the thin-film counterparts of these parameters. However, it is well established that thin films often exhibit deviations from bulk properties due to factors such as microstructure, surface effects, and deposition conditions. Recognizing this, we have evaluated the sensitivity of our results by introducing error bars that reflect a ± 10% variation in both density and specific heat capacity (see Figure 4(d)). This range represents a realistic estimate of possible deviations in thin-film properties and allows us to assess the potential uncertainty in our calculated ZT values (denoted as ZT_{appr}). For future work, we will use differential scanning calorimetry (DSC) and X-ray reflectivity (XRR) techniques to determine specific heat capacity and density of the thin films. Overall, these values are substantially lower than that of the bulk material, revealing κ ~11.1 $Wm^{-1}K^{-1}$ [56]. This distinct reduction highlights the effectiveness of nanostructuring in decreasing the thermal conductivity of Fe_2VAl compounds.

The reduction in the film's thermal conductivity compared to the bulk material is clearly a consequence of the differences in grain sizes. Additionally, the thermal conductivity decreases with decreasing thickness of the thin films, illustrating the effect of different grain sizes. The Wiedemann-Franz law is employed to evaluate the phonon part of the thermal conductivity [see supplementary information Table S1]. Adopting the aforementioned approximation for the thermal conductivity at elevated temperatures, the temperature-dependent thermal conductivity was calculated for $Fe_2V_{0.8}Mn_{0.2}Al$ samples. From that, an approximate figure of merit for ZT_{appr} was derived for all four samples, which are shown in Figure 4(d). The large power factor and relatively low values of thermal conductivity yields reasonably large values of the figure of merit (ZT_{appr} ~0.35), which are well above all other *p*-type bulk or thin film Fe_2VAl-based systems.

2. Thermoelectric properties of $Fe_2V_{0.9}Mn_{0.1}Al_{1.5}$ films for varying deposition temperatures

In addition, the thermoelectric properties of four thin films of Al-rich $Fe_2V_{0.9}Mn_{0.1}Al_{1.5}$ samples, employing different sputtering temperatures, have been studied. Figure 5(a–d) summarize the temperature-dependent thermoelectric properties of these Al-rich $Fe_2V_{0.9}Mn_{0.1}Al_{1.5}$ films. Obviously, the resistivity $\rho(T)$ of all off-stoichiometric films exhibit only modest temperature dependencies. Notably, the absolute values of $\rho(T)$ of the films deposited at RT and 200°C are larger than that of the 400°C and 600°C samples. This is, as already indicated, a direct consequence of the structural disorder present in the various specimens, which

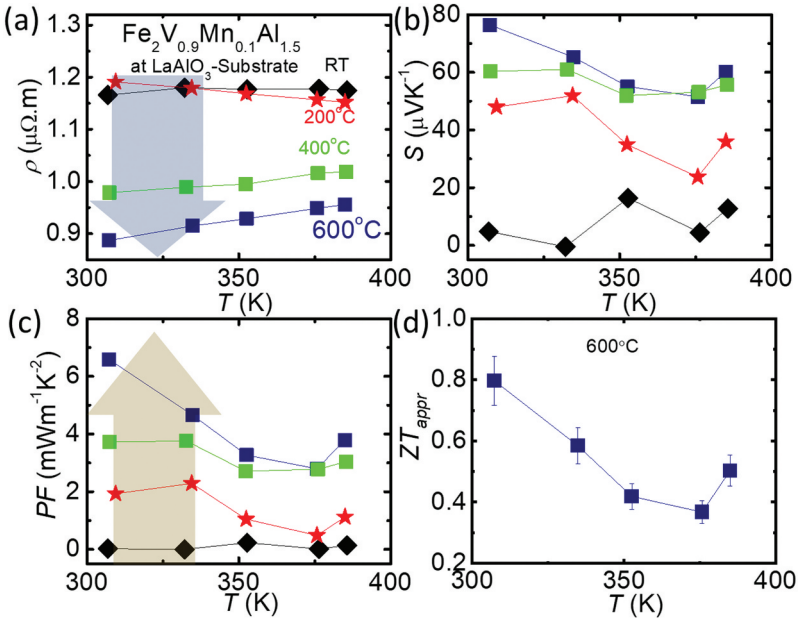

Figure 5. Electrical transport properties of $Fe_2V_{0.9}Mn_{0.1}Al_{1.5}$thin films deposited at different temperatures; RT, 200°C, 400°C, and 600°C, respectively; (a) electrical resistivity ρ, (b) Seebeck coefficient S, (c) the power factor *PF*, and (d) the figure of merit ZT_{appr}.

decreases with increasing deposition temperatures. In fact, the resistivity of the films decreases along the respective substrate temperatures, from the RT sample (lowest degree of structural order) to the 600°C sample (highest degree of structural order). Preferred orientation of grains is likely of less importance for these samples. Comparatively, the Al-rich $Fe_2V_{0.9}Mn_{0.1}Al_{1.5}$ thin films exhibit about 50% lower resistivity values than the $Fe_2V_{0.8}Mn_{0.2}Al$ films.

The Seebeck coefficient $S(T)$ of all $Fe_2V_{0.9}Mn_{0.1}Al_{1.5}$ films with varying deposition temperatures, show *p*-type behavior, too, indicating holes as majority charge carriers. $S(T)$ increases with increasing deposition temperature, revealing its largest value ($S = 79.5$ μVK^{-1}) for the sample deposited at 600°C, crystallizing in the ordered $L2_1$ structure. Aligning with the $\rho(T)$ results, there is a clear correlation of $S(T)$ values with the respective annealing temperature, most likely caused by the increasing structural order with increasing sputtering temperatures.

Additionally, modulation of the Al content in $Fe_2V_{0.9}Mn_{0.1}Al_{1.5}$ allows for further tuning of the carrier concentration and states. Density functional theory (DFT) studies on Al-rich $Fe_2V_{0.9}Mn_{0.1}Al_y$ indicate the emergence of localized electronic states on both sides of the Fermi level, along with a steeper energy dependence in the density of states [56]. Similar findings were observed experimentally by Parzer et al. on Al-rich Fe_2VAl systems, where a shift in the peak of the Seebeck coefficient versus carrier concentration was attributed to resonant states near the Fermi level [35]. In the present case, the combined Mn and Al doping in $Fe_2V_{0.9}Mn_{0.1}Al_{1.5}$ thin films likely induces similar resonant-like behavior via disorder, offering a fast and effective strategy to enhance the thermoelectric properties. Furthermore, higher deposition temperatures promote improved crystallinity, increased grain size, and reduced defect densities, which collectively enhance carrier mobility and further improve the thermoelectric performance of the films.

Consequently, the power factor (*PF*), depicted in Figure 5(c), is highest for the sample sputtered at 600 °C and reaches up to *PF* ~6.7 $mWK^{-2}m^{-1}$ at room temperature, marking a record-high value for any *p*-type Heusler thermoelectric materials, bulk or thin films [57,58]. A large power factor (~3.8 $mWK^{-2}m^{-1}$, $T = 300$ K), was also obtained for the film deposited at 400°C.

The thermal conductivity of the 600°C film is 2.54 $Wm^{-1}K^{-1}$ at room temperature, and therefore much lower than that of bulk of $Fe_2V_{0.9}Mn_{0.1}Al_{1.5}$ (~12 $Wm^{-1}K^{-1}$) [56]. The lower thermal conductivity of the thin film samples demonstrates the effectiveness of nano-structuring to decrease the thermal conductivity of Fe_2VAl systems. Thin films intrinsically have interfaces with the substrate and other layers and often feature internal defects like grain boundaries, as revealed in the SEM analysis. This establishes boundaries that scatter phonons more frequently, reducing their mean free path and consequently leading to a reduced thermal conductivity.

Assuming again a constant lattice thermal conductivity of $Fe_2V_{0.9}Mn_{0.1}Al_{1.5}$ near room temperature, allows to evaluate an approximated figure of merit ZT_{appr}, similarly as discussed above. Results are shown in Figure 5(d). Due to the combination of the large power factor and the reasonably low value of the thermal conductivity, an exceptional figure of merit $ZT_{appr} \sim 0.8$ is achieved at room temperature, which is more than four times larger than all other reported *p*-type bulk or thin film Fe_2VAl-based materials [57–59]. Notably, this is one of the highest *ZT* values ever reported at room temperature, coming even close to the figure of merit of Bi_2Te_3-based materials. Bi_2Te_3-based (Bi-Sb-Te) thin films still outperform Fe_2VAl films in terms of *ZT*, power factor, and thermal conductivity at room to moderate temperatures [60–64]. Although $Fe_2V_{0.9}Mn_{0.1}Al_{1.5}$ offers advantages in terms of stability and environmental friendliness, its thermoelectric (TE) performance lags behind, particularly at low to mid-temperature ranges relevant for wearable or ambient applications. Bi – Sb – Te thus remains the superior material for flexible, high-efficiency TE devices in this temperature regime [60–64]. Table S2 compares the typical *ZT* values and power factors of Bi – Sb – Te films with those of our $Fe_2V_{0.9}Mn_{0.1}Al_{1.5}$ films. Given that the constituent elements are reasonably inexpensive, and the material exhibits high chemical and mechanical stability, this represents a breakthrough in new material development and motivates further studies on these systems, including potential applications of full-Heusler materials in thin-film thermoelectric generators [65].

Magnetic properties, magnetotransport and TE enhancement mechanisms

To elucidate the origin of the enhancement of the thermoelectric performance observed for the Mn-doped films, magnetic properties are analyzed. Figure 6(a) depicts the temperature-dependent magnetization, *M*, of $Fe_2V_{0.8}Mn_{0.2}Al$, measured at $B = 0.1$ T for the 300 and 500 nm samples. For 300 nm film, the *M vs. T* curves exhibit paramagnetic behavior down to 2 K. In contrast, saturation of the magnetization is observed for the 500 nm film below 10 K. The temperature-dependent susceptibility, $M/\mu_0 H$, measured at $\mu_0 H = 1.0$ T, has been accounted for in terms of the Curie–Weiss relation $M/\mu_0 H = \chi = \chi_0 + C/(T - \theta_p)$, where $C = N\mu_{eff}/3k_B$, $\boldsymbol{x}_0$ is a temperature independent susceptibility contribution (fitted as $\boldsymbol{x}_0 = -0.00102$ emu/mol-Oe), and θ_p is the

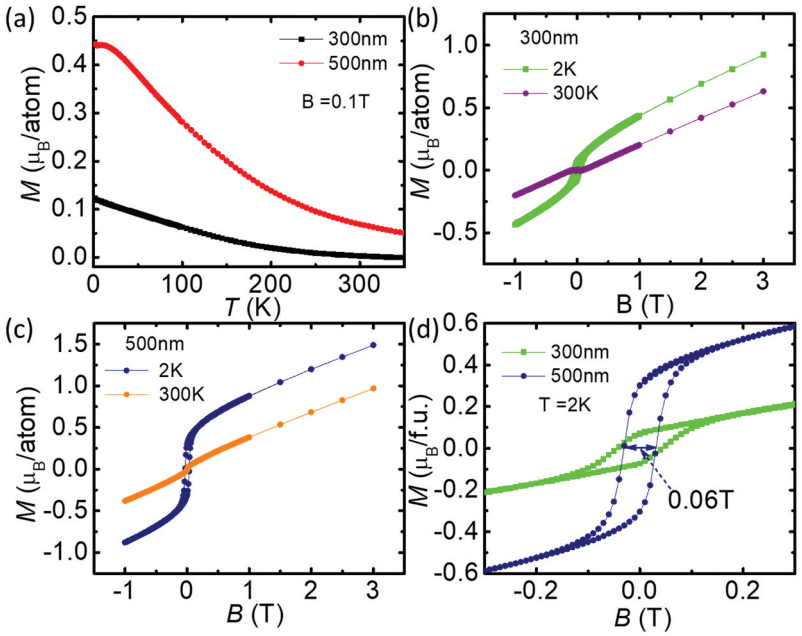

Figure 6. (a) Temperature dependence of magnetization of $Fe_2V_{0.8}Mn_{0.2}Al$ thin films of 300 nm and 500 nm thickness; (b–d) field dependence of the magnetization of $Fe_2V_{0.8}Mn_{0.2}Al$ thin films at 300 K and 2 K.

Weiss temperature [see Fig. S5(a, b)]. The values derived for the effective magnetic moment (μ_{eff}) are 2.04 μ_B and 2.46μ_B for the 300 and 500 nm films, respectively. The Weiss temperatures obtained are 381.5 and 134 K for the 300 and 500 nm film, respectively, indicating strong ferromagnetic interactions.

Figure 6(b,c) summarize isothermal *M vs* μ_0 *H* curves at 300 and 2 K for the 300 and 500 nm films, respectively. For the 300 nm film, the M vs H curve at 300 K exhibits a weak diamagnetic signal at low fields; at higher magnetic fields, *M* increases linearly with the applied field. At $T = 2$ K, *M vs* μ_0 *H* reveals weak ferromagnetism, together with a paramagnetic component. Similarly, the *M vs* μ_0 *H* curve for the 500 nm film shows a linear magnetic-field dependence at 300 K, with no diamagnetic signal in the low field region. As indicated from the *M vs* μ_0 *H* curve at $T = 2$ K, $Fe_2V_{0.8}Mn_{0.2}Al$ possesses a significant magnetic moment and a coercive field of 0.03 T.

The observed weak ferromagnetic behavior in both $Fe_2V_{0.8}Mn_{0.2}Al$ films and the notable ~60% higher magnetic moment in the 500 nm film indicate a clear thickness-dependent influence on magnetic ordering and the associated electronic band structure. Theoretically, it has been indicated that Mn atoms substituted at V sites exhibit significant localized magnetic moments (~2.43 μ_B), thereby confirming the famous Slater-Pauling rule, and introduce sharp impurity states near the band edges [56]. These states effectively narrow the pseudogap and pin the Fermi level near the valence band edge, leading to an asymmetric distribution of the density of states (DOS) around the Fermi energy. This asymmetry enhances the energy derivative of the conductivity (dlnσ/dE); as a result, the Seebeck coefficient becomes enhanced. The magnetic interactions between localized Mn moments further modify the spin-resolved electronic structure by inducing spin splitting of the conduction and valence bands. These effects are likely amplified in the thicker film due to improved crystallinity, facilitated by enhanced strain relaxation and reduced defect density. These structural improvements allow more coherent magnetic interactions and reduce spin-disorder scattering. As a result, the system exhibits stronger spin polarization and more pronounced band flattening, particularly in the majority spin channel, consistent with the experimentally observed increase in effective mass (*explained in the Hall effect section*). An increased effective mass corresponds to a higher DOS at the Fermi level, which enhances the Seebeck coefficient by increasing the number of thermally active states contributing to transport. Despite the nominal electron doping introduced by Mn substitution, DFT in Ref [56]. showed that the Fermi level remains within the pseudogap due to an accommodation of these electrons by localized Mn impurity states below E_F [56]. This prevents metallic behavior and supports high thermopower. Therefore, the combined effects of spin-dependent band modifications, Fermi level pinning, enhanced DOS asymmetry, and reduced scattering explain the improved thermoelectric performance observed in the thicker $Fe_2V_{0.8}Mn_{0.2}Al$ film, consistent with trends reported in other Mn-substituted Fe_2VAl systems [56].

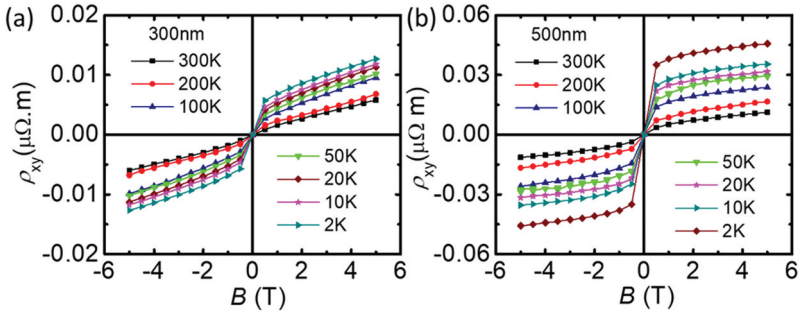

Figure 7. (a, b) Hall resistivity of $Fe_2V_{0.8}Mn_{0.2}Al$ thin films of thickness of 300 nm and 500 nm, respectively, at various temperatures.

In order to identify correlations between charge carrier transport and magnetic moments of $Fe_2V_{0.8}Mn_{0.2}Al$ films, the field- and temperature-dependent Hall resistivity was studied. Figure 7(a,b) shows the field-dependent Hall resistivity ρ_{xy} at various temperatures for the 300 nm and 500 nm films. Qualitatively, ρ_{xy} is different for magnetic (ferromagnetic) and nonmagnetic materials. In simple, nonmagnetic systems, ρ_{xy} increases linearly with applied fields B, as long as a single electronic band dominates. For ferromagnets, ρ_{xy} increases steeply in weak fields, but tends to saturate at higher magnetic fields. The saturation value is associated with the respective magnetization M. Commonly, the field-dependent Hall resistivity ρ_{xy} can be expressed as

$$\rho_{xy}(B) = \rho_{AHE} + R_H B. \quad (2)$$

The anomalous Hall resistivity, $\rho_{AHE} = 4\pi R_s M$, corresponds to the Hall effect contribution due to the material's intrinsic magnetization M. In Equation 2, R_H is the ordinary Hall coefficient that mainly depends on the density of carriers, while R_s represents the anomalous Hall coefficient. It quantifies the strength of the Hall voltage that arises due to the material's intrinsic magnetic properties.

The Hall resistivity obtained for $Fe_2V_{0.8}Mn_{0.2}Al$ films exhibits a distinct nonlinear behavior for all measured temperatures, indicating the existence of an AHE contribution in these films. Overall, a stronger AHE was observed for the 500 nm film, compared to the 300 nm sample. For both samples, the AHE becomes more dominant with decreasing temperature, and is strongest at 2 K. Overall, the AHE is weaker in the film samples compared to other bulk Heusler compounds, e.g. $Fe_2V_{0.9}Cr_{0.1}Al_{0.9}Si_{0.1}$ [36].

Since the saturation magnetization was not reached at fields of 5 T for any sample, ρ_{xy} data are accounted for according to Equation (2) Results are shown as solid lines in Figs S6 and S7. Numerical data obtained for ρ_{AHE} and R_H, are indicated in Figs. S4 and S5, too. For both samples, the anomalous term is weak near room temperature. The charge carriers are hole-type for both the 300 and 500 nm films, being consistent with the p-type Seebeck coefficient. Comparatively, the 500 nm film exhibits a slightly lower carrier concentration. Numerical values deduced at 300 K and 2 K for ρ_{AHE}, R_H, n_h are summarized in Table 2. The large AHE observed points to a strong coupling between the charge carriers and magnetism in $Fe_2V_{0.8}Mn_{0.2}Al$ thin films. We have noted before in a different system a large AHE accompanying an enhancement of the thermoelectric performance [39,42]. Here, the AHE contribution is strongest for the 500 nm $Fe_2V_{0.8}Mn_{0.2}Al$ sample, which also exhibits the highest PF of 4.26 $mWK^{-2}m^{-1}$ in the series.

As derived from XRD analysis, the lattice parameters of the ordered films are lower than those of the slightly disordered films. Simultaneously, the power factors of the highly ordered films are higher, suggesting that the ordered films with improved crystallinity exhibit higher TE performance. As observed from the SEM images, the grains are more distinct for the 500 nm film; comparatively, this sample outperforms the others. As the films were grown under similar conditions, the thickness dependence of the electronic and thermal transport can, most likely, be traced back to a higher degree of structural ordering and grain growth present in the

Table 2. The anomalous Hall effect (ρ_{AHE}), ordinary Hall coefficient (R_H), and carrier concentration (n_h) at 300K and 2K temperatures are presented here. The ordinary Hall coefficient (R_H) was extracted by linearly fitting the high-field part of ρ_H-B, as demonstrated in fig. S3 and S4.

Sample	T(K)	ρ_{AHE}(μΩ.m)	R_H (m^3/C)	n_h(m^{-3})
300 nm	300	0.056×10^{-2}	1.047×10^{-9}	5.97×10^{27}
	2.0	0.55×10^{-2}	1.46×10^{-9}	4.28×10^{27}
500 nm	300	0.47×10^{-2}	1.38×10^{-9}	4.51×10^{27}
	2.0	2.27×10^{-2}	1.9×10^{-9}	3.25×10^{27}

thicker samples, leading to improved TE properties. More precisely, when films have larger and well-connected grains, as seen in thicker samples, the phonon scattering decreases, allowing heat to flow more easily. This reduction in scattering improves the thermoelectric performance of the material by maintaining a better balance between electrical conductivity and thermal conductivity. Therefore, the improved TE properties in thicker films can be partially attributed to reduced phonon scattering due to larger grain sizes.

The Seebeck coefficient of the 500 nm thin film attains 108 μVK^{-1} at 300 K, which is the largest among all $Fe_2V_{0.8}Mn_{0.2}Al$ films. Microscopically, the enhancement of the Seebeck coefficient for the 500 nm thin film (up to 108 μVK^{-1} at 300 K) is due to increased carrier effective mass and decreased carrier concentration n_H. This follows from the application of Eqn. S1 to the experimental data. There, the Seebeck effective mass m_s is proportional to the Seebeck coefficient. The carrier concentration n_H was obtained from the Hall effect measurements [56]. As a result, m_s attains 11.4 m_0 and 15.19 m_0 for the 300 nm and 500 nm films, respectively, where m_0 is the free electron mass. Strong interaction between carriers and magnetism (magnetic drag effects, spin fluctuation, etc.) has led to increased effective mass and enhancement of Seebeck coefficient and power factor in various systems [36–42]. The increased carrier effective mass and large AHE observed here is consistent with a magnetic enhancement contributing to the high thermoelectric performance obtained.

Summary

In summary, high thermoelectric performance was found for *p*-type Mn-doped $Fe_2V_{0.8}Mn_{0.2}Al$ Heusler alloy thin films, grown on insulating oxide substrates. A large positive Seebeck coefficient, $S = 108\ \mu VK^{-1}$, is observed at $T = 300$ K for films of thickness 500 nm, facilitating a very large power factor of 4.26 $mWK^{-2}m^{-1}$. A clear thickness dependence was established for the TE performance of $Fe_2V_{0.8}Mn_{0.2}Al$ thin films (d = 100, 200, 300, and 500 nm). The largest *PF* was obtained for the well-ordered and well-crystallized 500 nm film. Films with thickness 300 and 500 nm revealed weak ferromagnetism, as obvious from magnetic measurements. Moreover, Hall data clearly indicate AHEs for these films. The AHE contribution is strongest for the 500 nm sample, also exhibiting the highest *PF* near room temperature. Note that even at $T = 300$ K, still a large AHE contribution is existent. The strong AHE which is indicative of strong interaction between the charge carriers and magnetism is likely to be an origin of the enhanced thermoelectric performance of Mn-doped $Fe_2V_{0.8}Mn_{0.2}Al$ Heusler thin films. Furthermore, we have achieved superior thermoelectric performance for Al-rich $Fe_2V_{0.9}Mn_{0.1}Al_{1.5}$ films deposited at different temperatures. The largest power factor, *PF* ~6.7 $mWK^{-2}m^{-1}$ and ZT_{appr} ~ 0.8 have been obtained at room temperature for $Fe_2V_{0.9}Mn_{0.1}Al_{1.5}$ films deposited at 600°C.

PF and ZT_{appr}, obtained in this study are, respectively, 1.5 times and 4 times larger than the best values ever reported for any bulk or thin film *p*-type Fe_2VAl-based material. The *PF* and ZT_{appr}, to the best of our knowledge, are also amongst the highest values ever reported for any thin-film-based *p*-type thermoelectric material. The outstanding room temperature values of *PF* and ZT_{appr} of Al-rich $Fe_2V_{0.9}Mn_{0.1}Al_{1.5}$ thin films substantially facilitate potential applications in energy harvesting, portable electronics, microelectronic devices, building energy efficiency, and self-powered sensors.

Disclosure statement

N.T., R.J., T.M. have filed one Japanese patent application (2024-079826) on the work described here. The remaining authors declare no competing interests.

Funding

This work was supported by JST Mirai Program, Grant number JPMJMI19A1. Authors (R.J. and N.T.) are grateful to the support by the Grand-in-Aid from Japan Society for the Promotion of Science (JSPS). Center support from JSPS WPI Academy is also thanked; JST-Mirai Program [JPMJMI19A1].

ORCID

Naohito Tsujii http://orcid.org/0000-0002-6181-5911
Takao Mori http://orcid.org/0000-0003-2682-1846

References

[1] Bell LE. Cooling, heating, generating power, and recovering waste heat with thermoelectric systems. Science. 2008;321(5895):1457–1461. doi: 10.1126/science.1158899
[2] Nandihalli LN, Liu CJ, Mori T. Polymer based thermoelectric nanocomposite materials and devices: fabrication and characteristics. Nano Energy. 2020;78:105186. doi: 10.1016/j.nanoen.2020.105186
[3] Petsagkourakisa I, Tybrandta K, Crispina X, et al. Thermoelectric materials and applications for energy harvesting power generation. Sci Technol Adv Mater. 2018;19(1):836–862. doi: 10.1080/14686996.2018.1530938
[4] Zhu T, Liu Y, Fu C, et al. Compromise and synergy in high-efficiency thermoelectric materials. Adv Mater. 2017;29(14):1605884. doi: 10.1002/adma.201605884
[5] Liu Z, Sato N, Gao W, et al. Demonstration of ultra-high thermoelectric efficiency of ~7.3% in Mg3Sb2/MgAgSb module for low-temperature energy harvesting. Joule. 2021;5(5):1196. doi: 10.1016/j.joule.2021.03.017

[6] Ambrosi RM, Williams H, Watkinson EJ, et al. European radioisotope thermoelectric generators (RTGs) and radioisotope Heater units (RHUs) for space Science and exploration. Space Sci Rev. 2019;215(8):55. doi: 10.1007/s11214-019-0623-9
[7] Hendricks T, Caillat T, Mori T. Keynote review of latest advances in thermoelectric generation materials, devices, and technologies 2022. Energies. 2022;15 (19):7307. doi: 10.3390/en15197307
[8] Pei Y, Shi X, LaLonde A, et al. Convergence of electronic bands for high performance bulk thermoelectrics nature. Nature. 2011;473(7345):66–69. doi: 10.1038/nature09996
[9] Mori T. Novel principles and nanostructuring methods for enhanced thermoelectrics. Small. 2017;13 (45):1702013. doi: 10.1002/smll.201702013
[10] Heremans JP, Jovovic V, Toberer ES, et al. Enhancement of thermoelectric efficiency in PbTe by distortion of the electronic density of states. Science. 2008;321(5888):554–557. doi: 10.1126/science.1159725
[11] Tan G, Zhao LD, Shi F, et al. High thermoelectric performance of p-type SnTe via a synergistic band engineering and nanostructuring approach. J Am Chem Soc. 2014;136(19):7006–7017. doi: 10.1021/ja500860m
[12] Wang L, Sato N, Peng Y, et al. Realizing high thermoelectric performance in N-Type $Mg_3(Sb, Bi)_2$-Based materials via Synergetic Mo addition and Sb–Bi ratio refining. Adv Energy Mater. 2023;13(35):2301667. doi: 10.1002/aenm.202301667
[13] Hinterleitner B, Knapp I, Poneder M, et al. Thermoelectric performance of a metastable thin-film heusler alloy. Nature. 2019;576 (7785):85–90. doi: 10.1038/s41586-019-1751-9
[14] Mikami M, Kinemuchi Y, Ozaki K, et al. Thermoelectric properties of tungsten-substituted Heusler Fe2VAl alloy. J Appl Phys. 2012;111 (9):093710. doi: 10.1063/1.4710990
[15] Kato H, Kato M, Nishino Y, et al. Effect of silicon substitution on thermoelectric properties of Heusler-type Fe2VAl alloy. J Jpn Inst Met. 2001;65:652. doi: 10.2320/jinstmet1952.65.7_652
[16] Nishino Y, Kato M, Asano S, et al. Semiconductorlike behavior of electrical resistivity in Heusler-type Fe2VAl compound. Phys Rev Lett. 1997;79(10):1909. doi: 10.1103/PhysRevLett.79.1909
[17] Feng Y, Rhee JY, Wiener TA, et al. Physical properties of Heusler-like Fe 2 VAl. Rev B. 2001;63(16):165109. doi: 10.1103/PhysRevB.63.165109
[18] Soda K, Murayama H, Shimba K, et al. High-resolution soft x-ray photoelectron study of density of states and thermoelectric properties of the Heusler-type alloys (Fe2/3V1/3)100–yAly. Phys Rev B. 2005;71:245112. doi: 10.1103/PhysRevB.71.245112
[19] Kato M, Nishino Y, Mizutani U, et al. Electronic, magnetic and transport properties of (Fe1-xVx) 3Al alloys. J Phys Condens Matter. 2000;12(8):1769–1779. doi: 10.1088/0953-8984/12/8/318
[20] Guo GY, Botton GA, Nishino Y. Electronic structure of possible 3d `heavy-fermion' compound Fe3Al. J Phys: Condens Matter 1998;10(8):L119. doi: 10.1088/0953-8984/10/8/002
[21] Singh DJ, Mazin II. Electronic structure, local moments, and transport in Fe2VAl. Phys Rev B. 1998;57(22):14352. doi: 10.1103/PhysRevB.57.14352
[22] Weht R, Pickett WE. Excitonic correlations in the intermetallic Fe2VAl. Phys Rev B. 1998;58(11):6855. doi: 10.1103/PhysRevB.58.6855
[23] Laila A, Nanko M, Takeda M. Preparation of eco-friendly Fe2VAl-based thermoelectric materials using cast iron scrap chips as a source material. Mater Trans. 2020;61:2216. doi: 10.2320/matertrans.mt-m2020197
[24] Lue CS, Ross JH. Semimetallic behavior in Fe2VAl: NMR evidence. Phys Rev B. 1998;58(15):9763. doi: 10.1103/PhysRevB.58.9763
[25] Weinert M, Watson RE. Hybridization-induced band gaps in transition-metal aluminides. Phys Rev B. 1998;58(15):9732. doi: 10.1103/PhysRevB.58.9732
[26] Okamura H, Kawahara J, Nanba T, et al. Pseudogap formation in the intermetallic compounds (Fe1–SxVx)3Al. Phys Rev Lett. 2000;84:3674. doi: 10.1103/PhysRevLett.84.3674
[27] Anand S, Gurunathan R, Soldi T. Thermoelectric transport of semiconductor full-Heusler VFe2Al. J Mater Chem C. 2020;8(30):10174. doi: 10.1039/D0TC02659J
[28] Berche A, Noutack MT, Doublet ML, et al. Unexpected band gap increase in the Fe2VAl Heusler compound. Mater Today Phys. 2020;13:100203. doi: 10.1016/j.mtphys.2020.100203
[29] Naka T, Sato K, Taguchi M, et al. Ferromagnetic quantum singularities and small pseudogap formation in Heusler type $Fe_{2+x}V_{1-x}Al$. Phys Rev B. 2012;85:085130. doi: 10.1103/PhysRevB.85.085130
[30] Jemima S, Mani A, Bharathi A, et al. Metal insulator transition in Fe2VAl1−xSix. J Alloys Compd. 2001;326:183–187. doi: 10.1016/S0925-8388(01)01245-2
[31] Amaladass EP, Satya AT, Sharma S, et al. Magnetization and magneto-transport studies on Fe2VAl1−xSix. J Alloys Compd. 2015;648:34–38. doi: 10.1016/j.jallcom.2015.06.229
[32] Nashima O, Kanomata T, Yamaguchi Y, et al. Magnetic and electrical properties of Fe3−xVxSi. J Alloys Compd. 2004;383:298–301. doi: 10.1016/j.jallcom.2004.04.061
[33] Garmroudi F, Riss A, Parzer M, et al. Boosting the thermoelectric performance of Fe2VAl–type Heusler compounds by band engineering. Phys Rev B. 2021;103(8):085202. doi: 10.1103/PhysRevB.103.085202
[34] Parzer M, Garmroudi F, Riss A, et al. High solubility of Al and enhanced thermoelectric performance due to resonant states in Fe2VAlx. Appl Phys Lett. 2022;120(7):071901. doi: 10.1063/5.0077159
[35] Jha R, Tsujii N, Bourgès C, et al. Thermoelectric properties of Cu-doped Heusler compound Fe2-xCuxVAl. Z Anorg Allg Chem. 2022;648(15): e202200058. doi: 10.1002/zaac.202200058
[36] Tsujii N, Nishide A, Hayakawa J, et al. Observation of enhanced thermopower due to spin fluctuation in weak itinerant ferromagnet. Sci Adv. 2019;5(2): eaat5935. doi: 10.1126/sciadv.aat5935
[37] Matsuura H, Ogata M, Mori T, et al. Theory of huge thermoelectric effect based on a magnon drag mechanism: application to thin-film Heusler alloy. Phys Rev B. 2021;104(21):214421. doi: 10.1103/PhysRevB.104.214421
[38] Ang R, Khan AU, Tsujii N, et al. Thermoelectricity generation and electron–magnon scattering in a natural chalcopyrite mineral from a deep-sea

hydrothermal vent. Angew Chem Int Ed. 2015;54 (44):12909. doi: 10.1002/anie.201505517
[39] Ahmed F, Tsujii N, Mori T. Thermoelectric properties of CuGa1−xMnxTe2: power factor enhancement by incorporation of magnetic ions. J Mater Chem A. 2017;5(16):7545. doi: 10.1039/C6TA11120C
[40] Zheng Y, Lu T, Polash MMH, et al. Paramagnon drag in high thermoelectric figure of merit Li-doped MnTe. Sci Adv. 2019;5(9):eaat9461. doi: 10.1126/sciadv.aat9461
[41] Vaney JB, Aminorroaya S, Yamini, et al. Magnetism-mediated thermoelectric performance of the Cr-doped bismuth telluride tetradymite. Mater Today Phys. 2019;9:100090. doi: 10.1016/j.mtphys.2019.03.004
[42] Hebert S, Daou R, Maignan A, et al. Thermoelectric materials taking advantage of spin entropy: lessons from chalcogenides and oxides. Sci Technol Adv Mater. 2021;22(1):583. doi: 10.1080/14686996.2021.1951593
[43] Uchida K, Takahashi S, Harii K, et al. Observation of the spin Seebeck effect. Nature. 2008;455 (7214):778–781. doi: 10.1038/nature07321
[44] Uchida K, Xiao J, Adachi H, et al. Spin Seebeck insulator. Nat Mater. 2010;9(11):894–897. doi: 10.1038/nmat2856
[45] Sakuraba Y. Potential of thermoelectric power generation using anomalous nernst effect in magnetic materials. Scr Mater. 2016;111:29–32. doi: 10.1016/j.scriptamat.2015.04.034
[46] Costache MV, Bridoux G, Neumann I, et al. Magnon-drag thermopile. Nat Mater. 2011;11(3):199–202. doi: 10.1038/nmat3201
[47] Vandaele K, Watzman SJ, Flebus B, et al. Thermal spin transport and energy conversion. Mater Today Phys. 2017;1:39–49. doi: 10.1016/j.mtphys.2017.05.003
[48] Boona SR, Watzman SJ, Heremans JP. Utilizing magnetization dynamics in solid-state thermal energy conversion. APL Mater. 2016;4(10):104502. doi: 10.1063/1.4955027
[49] Sakuraba Y, Hyodo K, Sakuma A, et al. Giant anomalous nernst effect in the Co2MnAl1−xSix Heusler alloy induced by Fermi level tuning and atomic ordering. Phys Rev B. 2020;101:134407. doi: 10.1103/PhysRevB.101.134407
[50] Maier S, Denis S, Adam S, et al. Order-disorder transitions in the Fe2VAl Heusler alloy. Acta Materialia. 2016;121:126–136. doi: 10.1016/j.actamat.2016.08.080
[51] Bandaru S, Jund P. Electronic structure of the Heusler compound Fe2VAl and its point defects by ab initio calculations. Phys Status Solidi (B). 2017;254 (2):1600441. doi: 10.1002/pssb.201600441
[52] Graf T, Felser C, Parkin SSP. Simple rules for the understanding of Heusler compounds. Prog Solid State Chem. 2011;39(1):1–50. doi: 10.1016/j.progsolidstchem.2011.02.001
[53] Jha R, Tsujii N, Garmroudi F, et al. Unexpected p-type thermoelectric transport arising from magnetic Mn substitution in Fe2V1−xMnxAl Heusler compounds. J Mater Chem C. 2024;12 (24):8861. doi: 10.1039/D4TC00779D
[54] Baba T, Taketoshi N, Yagi T. Development of ultrafast laser flash methods for measuring thermophysical properties of thin films and boundary thermal resistances. Jpn J Appl Phys. 2011;50:11RA01. doi: 10.1143/JJAP.50.11RA01
[55] Baba T. Analysis of one-dimensional heat diffusion after light pulse heating by the response function method. Jpn J Appl Phys. 2009;48(5S2):05EB04. doi: 10.1143/JJAP.48.05EB04
[56] Snyder GJ, Pereyra A, Gurunathan R. Effective mass from Seebeck coefficient. Adv Funct Mater. 2022;32 (20):2112772. doi: 10.1002/adfm.202112772
[57] Miyazaki H, Tanaka S, Ide N, et al. Thermoelectric properties of Heusler-type off-stoichiometric Fe2V1+xAl1−x alloys. Mater Res Exp. 2014;1(1):015901. doi: 10.1088/2053-1591/1/1/015901
[58] Kurosaki Y, Yabuuchi S, Nishide A, et al. Crystal growth and flat-band effects on thermoelectric properties of Fe2TiAl-based full-Heusler thin films. AIP Adv. 2020;10(11):115313. doi: 10.1063/5.0023660
[59] Nishino Y, Kamizono S, Miyazaki H, et al. Effects of off-stoichiometry and Ti doping on thermoelectric performance of Fe2VAl Heusler compound. AIP Adv. 2019;9(12):125003. doi: 10.1063/1.5123783
[60] Li Z, Yang X, Gao Z, et al. Remarkable average thermoelectric performance of the highly oriented Bi(Te, Se)-based thin films and devices. J Materiomics. 2024;10(2):366–376. doi: 10.1016/j.jmat.2023.06.008
[61] Fan P, Li R, Chen YX, et al. High thermoelectric performance achieved in Bi0.4Sb1.6Te3 films with high (00l) orientation via magnetron sputtering. J Eur Ceramic Soc. 2020;40(12):4016–4021. doi: 10.1016/j.jeurceramsoc.2020.04.059
[62] Qiu G, Li J, Ling Y, et al. Carrier concentration and orientation optimization for high performance (Sb, Bi)2Te3 thermoelectric films via magnetron co-sputtering. J Alloys Compd. 2023;950:169916. doi: 10.1016/j.jallcom.2023.169916
[63] Hu D, Liang S, He Y, et al. Effects of working pressure during magnetron sputtering on thermoelectric performance of flexible p-type Bi0.5Sb1.5Te3 thin films. J Vac Sci Technol B. 2024;42(3):032212. doi: 10.1116/6.0003631
[64] Zhang R, Jiang Q, Ye H. Enhancement of the thermoelectric performance of (BiSb)2Te3 films by single target sputtering. Ceram Int. 2024;50(14):24932–24938. doi: 10.1016/j.ceramint.2024.02.167
[65] Bourgault D, Hajoum H, Pairis S, et al. Improved power factor in self-substituted Fe_2VAl thermoelectric thin films prepared by co-sputtering. ACS Appl Energy Mater. 2023;6(3):1526–1532. doi: 10.1021/acsaem.2c03405